Title	Design and analysis of a contact-aided compliant force-limiting applicator mechanism for microneedle patches
Authors	Wang, Yiran;Dai, Shenyuan;Shi, Zhenjie;He, Xiuyun;Hao, Guangbo
Publication date	2026-06-05
Original Citation	Wang, Y, Dai, S, Shi, Z, He, X & Hao, G 2026, 'Design and analysis of a contact-aided compliant force-limiting applicator mechanism for microneedle patches', Journal of Mechanical Design, vol. 148, no. 11, 113307, pp. 1-11. https://doi.org/10.1115/1.4071942
Type of publication	Article (peer-reviewed)
Link to publisher's version	10.1115/1.4071942
Rights	© 2026, ASME. Reuse license: CC-BY 4.0. - https://creativecommons.org/licenses/by/4.0/
Download date	2026-09-22 05:27:43
Item downloaded from	https://hdl.handle.net/10468/19020

ASME Journal of Mechanical Design
Online journal at:
https://asmedigitalcollection.asme.org/mechanicaldesign

Design and Analysis of A Contact-Aided Compliant Force-Limiting Applicator Mechanism for Microneedle Patches

Yiran Wang
School of Engineering and Architecture,
University College Cork,
Cork T12 K8AF, Ireland
e-mail: 123112682@umail.ucc.ie

Shenyuan Dai
Key Laboratory of AI Agents for Agriculture,
Wenzhou Academy of Agricultural Sciences,
Wenzhou 325006, China
e-mail: b20200255@xs.ustb.edu.cn.

Zhenjie Shi
School of Engineering and Architecture,
University College Cork,
Cork T12 K8AF, Ireland;
School of Mechanical Engineering,
Shandong University,
Jinan 250100, China
e-mail: shizhenjie@mail.sdu.edu.cn

Xiuyun He
Photonics Center,
Tyndall National Institute,
Cork T12 R5CP, Ireland
e-mail: xiuyun.he@tyndall.ie

Guangbo Hao[1]
School of Engineering and Architecture,
University College Cork,
Cork T12 K8AF, Ireland
e-mail: g.hao@ucc.ie

Microneedle patches are emerging minimally invasive devices that deliver drugs using micron-scale needles to penetrate the stratum corneum of the skin, offering significant advantages such as minimal pain, convenient administration, and low risk of infection. However, microneedle patches are typically applied by thumb pressing, making it difficult to limit the maximum input force, which can cause needle damage or even nerve contact causing pain. This article proposes a force-limiting applicator for microneedle patches, which limits the maximum input force through a sheet-based contact-aided compliant force-limiting mechanism (CCFM). The sheet-based CCFM consists of a compliant sheet and a contact rod (with smooth contact surface). As the contact surface contacts the compliant sheet, causing it to deform, the reaction force gradually increases. When the contact surface separates from the compliant sheet, the deformation disappears, leading to a sudden reduction in the reaction force. The sheet-based CCFM contains no electronics, making the applicator easy to miniaturize, reusable, and cost-effective. In addition, by designing different dimensions of the compliant sheet and contact surface, the applicator can satisfy various force-limiting requirements. The chained pseudo-rigid-body model (CPRBM) is used to predict the deformation of the compliant sheet in contact with linear and curved contact surfaces. The model is validated using finite element analysis (FEA), with maximum relative errors of 6.61% and 6.79%, respectively. The reaction force is obtained using the Lagrange multiplier method. For the two different contact surfaces, the maximum relative errors between the analytical and FEA results are 9.3% and 6.8%. In addition, physical prototypes are manufactured and experimental tests are performed to further verify the feasibility of the design. Finally, the design procedures, the limitation of the analytical model, and future work are discussed.
[DOI: 10.1115/1.4071942]

Keywords: contact-aided compliant mechanism, force limiting mechanism, medical device, chained pseudo-rigid-body model

Introduction

Force limitation and force feedback are essential in sensitive operations, such as minimally invasive surgery, medical rehabilitation equipment, and human–robot interaction [1–3]. In machinery, it is difficult to replicate this force feedback in a reliable and inexpensive manner without sacrificing speed, simplicity, or productivity. For humans, this force feedback comes naturally and is developed through experience; however, in the case of minimally invasive surgery or any other sensitive operation toward the human body, excessive force can cause irreparable damage to sensitive tissues [4]. A representative example is microneedle injection. Microneedles are typically mounted on a patch that consists of hundreds of micron-scale needles arranged in an array, which are extremely fragile and highly sensitive to force. The required insertion force varies between individual microneedles, and excessive force can damage the needles, leading to drug leakage, or more seriously, cause the needle tips to contact nerves, resulting in pain. Therefore, it is crucial to design a device capable of controlling the maximum input force for microneedle patch applications [5–7].

The majority devices that achieve force feedback or force-limiting functionality rely primarily on force sensors or precision mechanical components [8–10]. The former monitors the force in real time through electronics, while the latter achieves overload protection through precise structural design. However, both methods either require a sophisticated control system and expensive electronic components or rely on advanced manufacturing and assembly techniques. This increases both cost and complexity, making their application in miniature or low-cost devices limited.

[1]Corresponding author.

The original version of this paper has been accepted to be presented in ASME IDETC/CIE 2025 with a reference number: 169339.

Contributed by the Mechanisms and Robotics Committee of ASME for publication in the Journal of Mechanical Design. Manuscript received December 22, 2025; final manuscript received April 20, 2026; published online June 5, 2026. Assoc. Editor: Dan Zhang.

The application of compliant mechanisms (CMs) in force-limiting and force-sensing devices can greatly address the aforementioned issues. CMs utilize the elastic deformation of their flexible components to transfer force and motion, compared to traditional rigid mechanisms, CMs offer significant advantages such as being frictionless, requiring no lubrication, and easily miniaturized with low manufacturing costs [11]. At present, some work has been done on robot sensing and microelectromechanical systems using CMs to assist in force sensing or force limiting. Wei et al. [12] presented a 1-D force sensor with mN resolution using multiple parallel antiparasitic motion flexure blades to inject cells with enough accuracy. Chen and Lan [13] designed an adjustable constant force mechanism, which is used to passively regulate the contact force of a robot's end effector. Pham and Wang [14] developed another bistable constant force mechanism that can realize constant contact force and overload protection. Zhang et al. [15] proposed a quasi-constant force mechanism based on curved beams, which is applied in flexible robotic hands and force-sensitive manipulation. Miao and Zheng [16] designed an apple picker robot, which achieved the required constant output force by incorporating a compliant mechanism in the end effector.

The buckling of compliant elements is also widely applied in force-sensing and force-limiting applications. Slocum et al. [17] designed a monolithic force-limiting flexure and applied to a toothbrush. The buckling flexure employs a twin-beam structure with an upper beam that includes a nesting arch on its underside and a lower buckling beam member which buckles when excessive force is applied to the tip, but restores to its original shape when the force is relieved. In the study by Dobrokhotov et al. [18], buckled shapes are visually used to determine force on a nanoscale, in which a 15.6 μm wire or "needle" is developed to probe nanofibers and other structures of similar size. An et al. [19] developed a nonlinear buckling sensor for devices such as seismometers. By monitoring the shape changes of a preloaded cantilever beam, the sensor provides real-time data output. Noda et al. [20] designed a force limiter based on a leaf spring bending mechanism, installed on surgical forceps for minimally invasive surgery. Similar work has been done by Heimberge and Schaumann [21], who used force-limiting components made of super-elastic materials, also applied in medical clamps. These force-limiting components connect the handle end to the clamp, transmitting and limiting the force applied by the user.

The force-sensing and force-limiting devices based on contact-aided compliant mechanisms (CCMs) have also seen significant development. The CCM was first proposed by Mankame and Ananthasuresh [22]. Unlike traditional compliant mechanisms, CCMs utilize mutual contact with rigid external objects and/or internal self-contact with different parts to generate nonsmooth output trajectories and load–deflection characteristics. Force-limiting and force-sensing mechanisms based on CCMs typically induce deformation in flexible components through rigid external bodies to sense or control force. Saxena [23] presented a monolithic contact-aided displacement-delimited gripper, which limits the output displacement through contact interactions between deformable components, thereby preventing the application of excessive force. Yao et al. [24] designed a compliant intrinsic force-sensing gripper that obtains the force–displacement relationship through contact between the object and the compliant beam, and provides real-time feedback on the reaction force. CCMs have been extensively developed and applied in diverse mechanical and robotic applications. However, to the best of our knowledge, the majority existing CCMs are designed to achieve variable stiffness, whereas studies on CCMs capable of providing force relief or force-limiting remain scarce, especially in the field of medical device applications.

This article introduces a sheet-based contact-aided compliant force-limiting mechanism (CCFM), which is integrated into a microneedle patch applicator to limit the maximum input force of microneedle patches. The proposed sheet-based CCFM only consists of two parts: a compliant sheet and a contact rod. By allowing the compliant sheet to contact the head of the contact rod, the compliant beams within it undergo varying degrees of bending deformation, thereby limiting the maximum input force. This design offers several advantages, including structural simplicity, ease of miniaturization, reusability, low manufacturing cost, and convenient operation. The analytical model is established based on the chained pseudo-rigid-body model (CPRBM). In the analytical model, the sheet-based CCFM with different compliant sheet dimensions and contact surfaces can be configured to achieve various force-limiting requirements, significantly enhancing the design efficiency.

The remainder of this article is organized as follows. Section 1 provides a detailed introduction to the structure and force-limiting principle of the proposed microneedle patch applicator. Section 2 develops the analytical model of the sheet-based CCFM through the CPRBM and introduces a method to obtain the force–displacement relationship by extracting the Lagrangian operator. Section 3 analyzes two design examples through numerical analysis and finite element analysis (FEA). Section 4 proceeds with an experimental test to further verify the proposed mechanism. The discussions and conclusions are presented in Secs. 5 and 6.

2 Design of the Contact-Aided Compliant Force-Limiting Applicator Mechanism

The force-limiting microneedle patch applicator should satisfy two design requirements: dimensional requirements and force-limiting requirements. The dimensional requirements specify that the applicator should have a simple and compact structure, be easy to carry, and allow one-handed operation. The force-limiting requirements specify that, under a prescribed input displacement, the applicator must reach a maximum allowable input force that does not increase further with additional displacement. This requirement is achieved through the sheet-based CCFM. Taking into account the average size of the adult hand and the ergonomic grip comfort, the overall shape of the force-limiting applicator is designed as a cylinder, with a height of $H = 60$ mm and a diameter of $D = 20$ mm, as shown in Fig. 1. The force-limiting applicator includes six parts: base, outer cylinder, guide rod, contact rod, compliant sheet, and upper cylinder. The base is aligned with the microneedle patch and is positioned at the bottom of the applicator. The outer cylinder is equipped with a guide groove that interfaces with the guide rod, preventing it from falling. A blade-shaped structure at the upper end of the guide rod is inserted into the slot of the outer cylinder, restricting rotational motion while allowing smooth vertical translation within the cylinder. The contact rod is fixed at the topmost point of the guide rod, precisely at the center of the blade structure, and moves vertically in unison with the guide rod. The compliant sheet is secured between the outer cylinder and the upper cylinder, with its three compliant beams aligned with the corresponding gaps in the inner wall of the outer cylinder. The upper cylinder is positioned above the compliant sheet, providing additional fixation and structural stability.

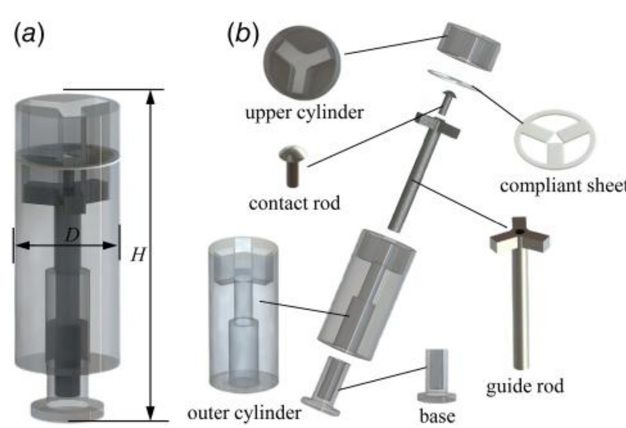

Fig. 1 Force-limiting microneedle patch applicator: (*a*) overall structure and (*b*) structural components

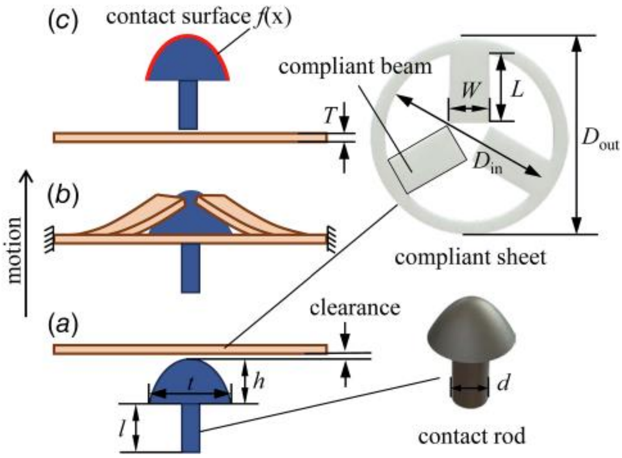

Fig. 2 The sheet-based CCFM: (*a*) initial phase, (*b*) contact phase, and (c) separation phase

The compliant sheet and the contact rod collectively constitute the sheet-based CCFM. The working principle of this mechanism is illustrated in Fig. 2. In the initial phase, the compliant sheet is mounted above the contact rod with a 0.2-mm clearance (defined as the distance between the top end of the compliant rod and the compliant sheet). As the rod moves upward, it contacts the compliant sheet and induces bending deformation in its three compliant beams, generating a reaction force on the rod. The continued upward motion of the rod increases the beam deformation and thus the reaction force until the beam reaches the maximum contact point, where the reaction force attains its peak value. Beyond this point, further upward displacement causes the rod to lose contact with the sheet, eliminating the bending deformation and allowing the sheet to return to its original state, resulting in a rapid drop of the reaction force to zero. This movement realizes the force-limiting function. The profile of the contact rod head surface is a continuous and smooth curve to ensure that the reaction force increases gradually and continuously.

When using the force-limiting applicator, the microneedle patch is first attached to the base. Then hold the outer cylinder of the applicator and apply a downward input displacement d_{in}, shown in Fig. 3. The applied d_{in} causes the guide rod to move upward and allows the contact rod to contact the compliant sheet, inducing bending of the compliant beams. The reaction force generated by the bending of the compliant beams is transmitted through the contact rod to the base and then to the microneedle patch. Therefore, the reaction force is the insertion force for the microneedle patch. When the contact rod separates from the compliant sheet, a crisp "click" sound is produced due to friction and the deformation of the compliant sheet, alerting the user that the maximum input force has been reached. Pulling down the base resets the contact rod to its initial position, enabling the applicator to be reused.

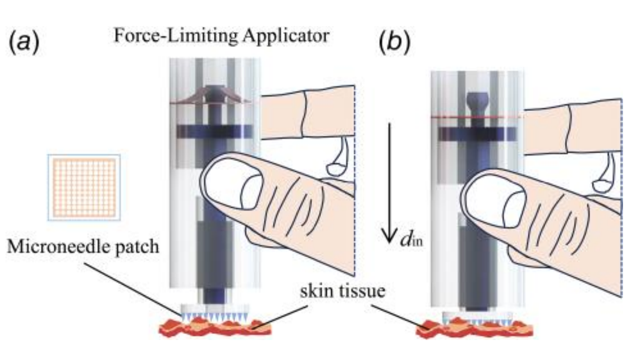

Fig. 3 Scenarios of proposed force-limiting microneedle patch applicator: (*a*) injection and (*b*) injection completed

3 Modeling and Analysis

The contact phenomenon in CCMs introduces strong boundary nonlinearities, in order to analyze the sheet-based CCFM, it is necessary to introduce a method for large-deflection analysis. Among the various analytical methods [25–27], the CPRBM method [28,29] has been widely adopted due to its relatively simple modeling principles. Moreover, the CPRBM is more straightforward for 2D problems and is also easy to embed contact constraints into the deformation analysis. Therefore, this study employs the CPRBM to develop the analytical model of sheet-based CCFM.

3.1 Chained Pseudo-Rigid-Body Model. In CPRBM, rigid members with an equivalent force–deformation relationship are used to simulate flexible members, as shown in Fig. 4, where Δx and Δy denote the displacement of the beam end along x-axis and y-axis, respectively, and $\Delta \phi$ denotes the rotation angle of the beam end. The compliant beam is divided into multiple flexible segments, each of which can be modeled as a series of tiny rigid elements which are connected end to end through torsional springs. The force–deflection relationship of each segment is accurately represented by the spring attached at the joint. By determining the positions of the joints and the value of the corresponding spring constants, the deformation trajectory of the beam can be effectively predicted. The stiffness constant k_i of each torsional spring is approximately calculated as

$$k_i = \frac{EI}{L_i}, \quad i = 1, 2, \ldots, N \tag{1}$$

where EI is the bending stiffness of the beam element, L_i is the length of the ith rigid element, and N is the number of rigid

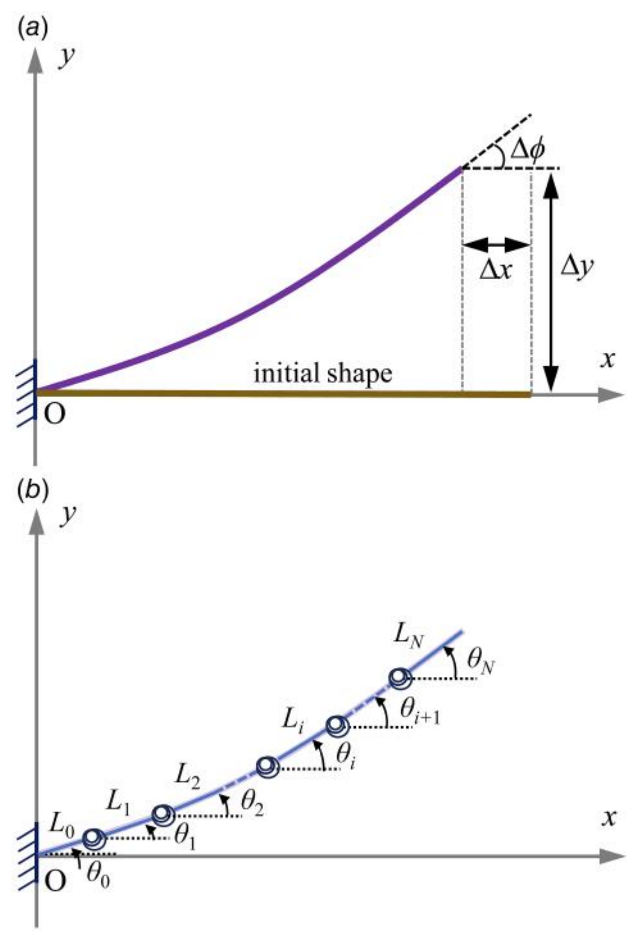

Fig. 4 Modeling schematic of CPRBM: (*a*) curved beam and (*b*) its chained pseudo-rigid-body model

elements. When the number of elements N is large enough, the resulting CPRBM can equivalently describe the nonlinear load-deflection characteristics of the flexible beam. Not only can the beam's end position but also their deformed shapes be accurately described.

Without contact interaction, the static equilibrium problem of the CPRBM is formulated based on the principle of minimum potential energy PE [30,31]. When the potential energy of a system is minimum, the system will be in a stable equilibrium state. By minimizing PE of the compliant system under the constraints of the vector loop equation(s), $\mathbf{Z}(\theta_1, \theta_2, \ldots, \theta_N) = 0$, the static equilibrium position of the CPRBM, i.e., the deformed state of the beams can be obtained. The vector loop equation is used for cases in which one end of the compliant beam is fixed.

$$\begin{aligned} \min \quad & PE \\ \text{s.t.} \quad & \mathbf{Z}(\theta_1, \theta_2, \ldots, \theta_N) = 0 \end{aligned} \tag{2}$$

For the displacement-loaded condition, the potential energy PE only contains the strain energy of the whole system, which is the elastic energy stored in the deformed structure, shown as follows:

$$PE = \sum_{i=1}^{N} \frac{1}{2} k_i \delta_i^2 \tag{3}$$

where δ_i denotes the rotation angle of the ith torsional spring and is calculated as $\delta_i = (\theta_i - \theta_{i-1}) - (\theta_i^{'} - \theta_{i-1}^{'})$. θ_i and $\theta_i^{'}$ are the final and initial tangent angles of the ith element, respectively.

3.2 Formulation of Contact Problems. The contact in CCMs is divided into compliant–compliant contact and compliant–rigid contact. Because the contact rod in the sheet-based CCFM is a rigid body, it is a compliant–rigid contact. To describe the interaction between the compliant element and the rigid body, some boundary conditions should be added. First, define the contour curve of the rigid body surface as a continuous function $f(x)$. The position of the connection point for each small segment of the deformed beam can be calculated as

$$x_i = \sum_{j=0}^{i-1} L_j \cos(\theta_j), \quad y_i = \sum_{j=0}^{i-1} L_j \sin(\theta_j) \tag{4}$$

The corresponding coordinates for each connection point are (x, y), and its projection point along the y-axis on the contact surface $f(x)$ is $(x_i, f(x_i))$, as shown in Fig. 5. The contact surface is simulated by the polynomial curve [32], which function is continuous, explicit, and relatively simple. The polynomial curve is generated by multiple points, starting with defining the coordinates of the control points $C_i(x_{ci}, y_{ci})$, $i = 1, 2, \ldots, N_c$, where N_c denotes the number of control points. By fitting the control points with a polynomial curve, the profile function of the contact surface can be defined as

$$f(x) = a_{N_P} x^{N_P} + a_{N_{P-1}} x^{N_{P-1}} + \cdots + a_1 x + a_0 \tag{5}$$

where N_P is the order of the polynomial function and $N_P = N_c - 1$. If the contact surface is a continuous straight line, only two control points are required. If the contact surface is a smooth quadratic curve, three control points need to be defined. This approach enables designers to explore a wider range of potential design solutions without requiring a predefined geometric configuration. By adjusting the positions of control points, the contact surface can be modified without the need to explicitly define a mathematical function. This article does not provide an in-depth study of profile curves, and the pros and cons of alternative curves are open to exploration.

Second, confined the deformation of the flexible beam to the outside of the rigid contact surface, a contact constraint $g(x_i, y_i)$ is introduced to describe the distance between the connection points of each small segment and the contact surface. When the contact region is below the compliant elements, the related joints should be above their corresponding projection points. Hence, the contact constraint $g(x_i, y_i)$ can be formulated as

$$g(x_i, y_i) = f(x_i) - y_i \le 0, \quad i \in [a, b] \tag{6}$$

where $[a, b]$ represents the region of joints that may contact the rigid surface. In addition, the number of contact constraints should be equal to the number of relevant joints.

Then, add the contact constraints to Eq. (2), the deformed flexible beam in rigid contact can be described. The specific mathematical model can be formulated as

$$\begin{aligned} \min \quad & PE \\ \text{s.t.} \quad & \mathbf{Z}(\theta_1, \theta_2, \ldots, \theta_N) = 0 \\ & g(x_i, y_i) \le 0, \quad i \in [a, b] \end{aligned} \tag{7}$$

3.3 Calculation of the Reaction Force At Input Port. The input port of CCMs can be actuated by force or displacement. In sheet-based CCFM, a downward displacement along the y-axis is applied to the input port, which is located at the left end of the compliant beam, as illustrated in Fig. 6. According to the force equilibrium condition, the reaction force at the input port is the contact force generated between the compliant beam and the contact rod, which also represents the force applied to the microneedle patch. Then, the analysis problem is to find the deformation and reaction force of the mechanism based on a known input displacement. By solving the constrained minimum problem in Eq. (7), the deformed configuration of the beam can be obtained directly. Furthermore, the reaction force corresponding to the input displacement is also readily available, as it is incorporated into the Lagrange equations of the optimization process. In our previous work [33], the energy method was employed to solve for the reaction force. Compared to

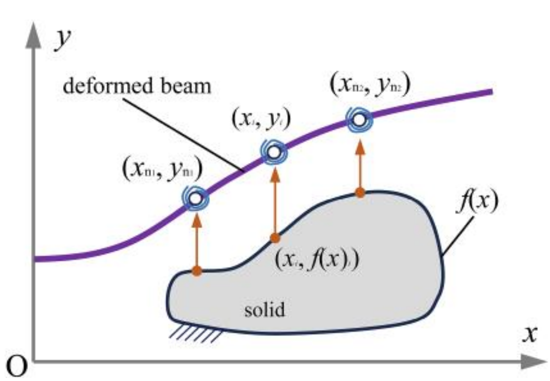

Fig. 5 Schematic representation of the contact constraints on the deformed beam

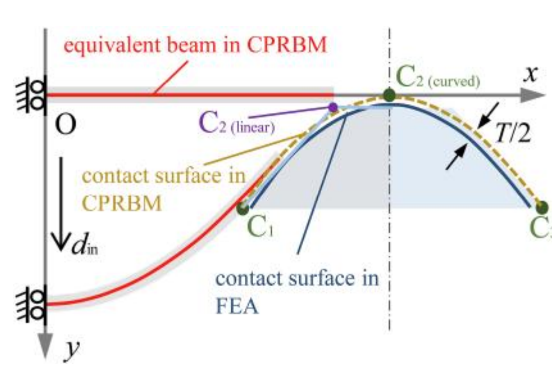

Fig. 6 Schematic of the FEA simulation for the sheet-based CCFM

the energy method, the *fmincon* algorithm based on the Karush–Kuhn–Tucker (KKT) conditions used in this article explicitly extracts the Lagrange multipliers during the solution of Eq. (7), allowing the reaction force at the input port to be obtained without additional computations. The established mathematical model Eq. (7) is a nonlinear constrained optimization problem, which can be solved using the optimization algorithm *fmincon* in MATLAB. The constraint handling mechanism of *fmincon* is based on the Lagrangian function formulated under the KKT conditions [34], where the gradients of both the objective function and the constraint functions are jointly considered. Specifically, to handle the inequality constraints in Eq. (7), *fmincon* introduces the Lagrange multiplier λ and constructs the Lagrangian function as follows:

$$\mathcal{L}(X, \lambda) = \Pi(X) + \sum_{i \in C} \lambda_i g_i(X) \tag{8}$$

where $\Pi(X)$ represents the total potential energy of the compliant beam, C denotes the set of potential contact points, and λ_i is the corresponding Lagrange multiplier. In optimal conditions, for any contact point i:

$$\frac{\partial \mathcal{L}}{\partial X} = \nabla \Pi(X) + \sum_{i \in C} \lambda_i^* \nabla g_i(X) = 0 \tag{9}$$

That is, the gradient of the total potential energy combined with the "reaction forces" along the constraints' directions sums to zero. In conjunction with the KKT conditions,

$$\lambda_i^* \geq 0, \quad g_i(X^*) \leq 0, \quad \lambda_i^* \cdot g_i(X^*) = 0 \tag{10}$$

These three conditions ensure that the solution X^* is both optimal and physically valid. Here, λ_i^* represents the magnitude of the contact force, while $\nabla g_i(X)$ specifies its direction. The KKT conditions imply that a contact force exists only if the contact point is exactly on the rigid surface (i.e., $g_i(x_i, y_i) = 0$). In this case, $\lambda_i^* > 0$ represents the reaction force required to maintain contact at that point. Conversely, when there is no contact (i.e., $g_i(x_i, y_i) < 0$), that is, $\lambda_i^* = 0$, indicating the absence of contact force. This interpretation of the multipliers as reaction forces provides a physically meaningful way to extract contact forces from a constrained energy-based optimization framework.

4 Case Study

The microneedles used in this study are dissolvable microneedles [35] with a pentagonal structure and are fabricated from the drug itraconazole. They are specifically designed for nail skin injection, with heights 500 μm and 700 μm. Because dissolvable microneedles are composed entirely of the therapeutic agent itself and subsequently dissolve to release the medication after penetrating the stratum corneum layer of the skin, they require greater precision in the injection force. To achieve effective transdermal drug delivery, approximately 70–80% of the microneedle length must penetrate the skin. However, the mechanical properties of skin vary significantly with factors such as sex, age, and anatomical location. In general, thumb pressing typically generates an insertion force of approximately 3–6 N when applying microneedles [36,37]. Therefore, this study sets the maximum input force for the microneedle patch at 5–6 N to represent a general scenario. Furthermore, considering the dimensional requirements of the applicator, the input displacement corresponding to this maximum force is set to 5 mm. This establishes the force-limiting requirement: at an input displacement of 5 mm, the maximum input force should be within 5–6 N.

The designed compliant sheet is circular and contains three identical straight beams arranged in circular symmetry. The contact surface of the contact rod also has a regular symmetric structure. To simplify theoretical analysis, one compliant beam and half of the contact surface are selected to establish the analytical model. Based on the diameter D of the microneedle patch applicator, the outer diameter of the compliant sheet is defined as $D_{\text{out}} = 20$ mm. To accommodate the arrangement of three straight compliant beams, each beam is designed with a length of $L = 7$ mm and a width of $W = 4$ mm. Considering the combined requirements of specific strength, stiffness, and fatigue resistance, PEEK is selected as the material for the compliant sheet, with Young's modulus $E = 3600$ MPa, Poisson's ratio $\mu = 0.38$, and yield strength $\sigma_y = 110$ MPa. The thickness of the compliant beam is set as 0.3, 0.4, and 0.5 mm for further analysis. For the contact rod, the contact surfaces are designed as linear and curved types, respectively. The contact head of the contact rod with linear contact surface has a trapezoidal cross section. The apex of the contact surface is defined by the control point C_2, while its width t is determined by C_1 or both C_1 and C_3, shown in Fig. 6. In CPRBM, the compliant beam is horizontally aligned along the x-axis, with the midpoint of its left end coinciding with the origin of the coordinate system, as illustrated in Fig. 6. For sheet-based CCFM, a clearance must be reserved between the compliant sheet and the contact rod to prevent premature contact. Therefore, for the linear contact surface, C_2 is defined as (7, −0.2), indicating that the contact surface is positioned directly beneath the compliant beam with a clearance of 0.2 mm. For the curved contact surface, due to its curvature, the apex C_2 is defined to coincide with the midpoint of the compliant sheet, i.e., C_2 (8.4, 0). To analyze the effect of different contact surface widths on the reaction force, C_1 is defined as (4.5, −2.5), (5, −2.5), and (5.5, −2.5), respectively. Since C_3 is symmetric to C_1 about the centerline of the compliant sheet, the corresponding C_3 is (12.3, −2.5), (11.8, −2.5), and (11.3, −2.5). Taking C_1 (5, −2.5) and C_3 (11.8, −2.5) as an example, substituting these control points into Eq. (5), the linear contact surface $f(x)_{\text{line}}$ and the curved contact surface $f(x)_{\text{curve}}$ are formulated as

$$f(x)_{\text{linear}} = 1.15x - 8.25 \tag{11}$$

$$f(x)_{\text{curved}} = -0.2163x^2 + 3.6332x - 15.2595 \tag{12}$$

By substituting Eqs. (11) and (12) into Eq. (7), two theoretical analytical models are established. In CPRBM of the sheet-based CCFM, the number of joints is set as $N = 100$.

For nonlinear FEA simulation, 2D models are created and imported into ANSYS WORKBENCH 2024 R2. Since the analytical model does not account for friction, the contact type in FEA is defined as frictionless to better compare the analytical results. The contact behavior is defined as asymmetric, and the Lagrange formulation is selected. Setting the default triangular mesh element and the normal-level meshing techniques (9.33-mm bounding box diagonal, 2.31-mm average surface area, 1.2 growth rate, 5 maximum layers, and 0.27 overhang ratio). Refine the mesh for the two contact surfaces individually, adjusting the element size to 0.1 mm (smaller than the thickness of compliant beam) and applying local mesh refinement to the contact surfaces. It should be noted that the CPRBM simulates the centerline of the compliant beam. In FEA, the contact surface should be offset downward by $T/2$ mm, which is half the thickness of the compliant beam. In Fig. 6, the centerline of the compliant beam represents the equivalent beam modeled using the CPRBM. When the compliant beam contacts the FEA contact surface, the equivalent beam also makes contact with the CPRBM contact surface. This accordingly simulates the state of the compliant beam that contacts the real contact surface.

The deformation interaction of the sheet-based CCFM with the linear contact surface is shown in Fig. 7(*a*), and the displacement of the beam tip along y-axis for different input displacements is shown in Fig. 7(*b*). For the curved contact surface, the two results are shown in Fig. 8. For the linear contact surface, the maximum relative error between the CPRBM and FEA results is 6.61% at an input displacement of 2 mm, whereas for the curved contact surface, the corresponding relative error is 6.79% at an

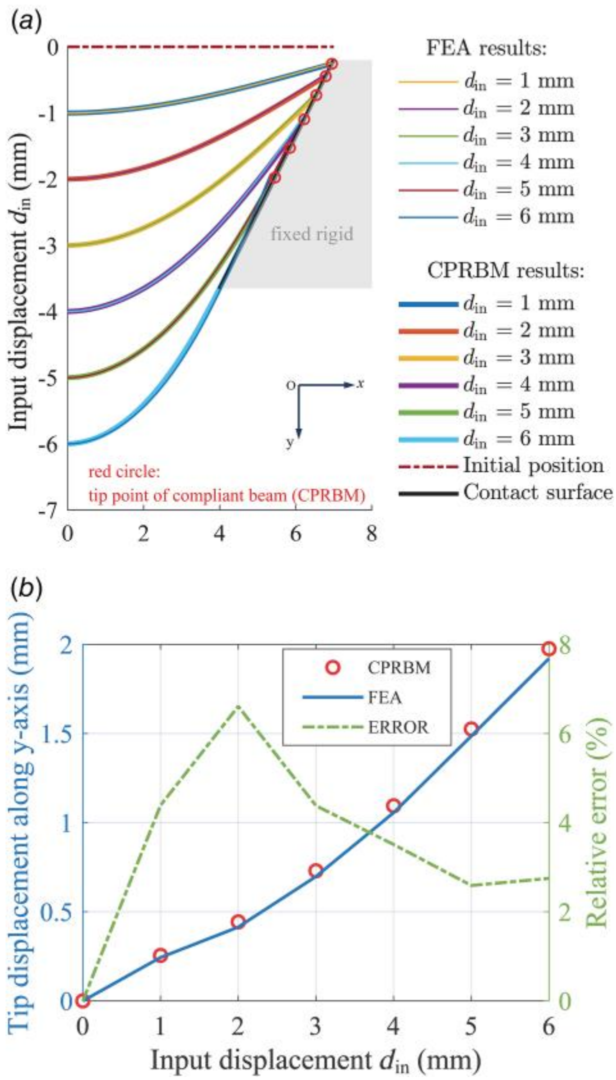

Fig. 7 Sheet-based CCFM with linear contact surface: (*a*) compliant beam interaction with linear contact surface and (*b*) its tip displacement along y-axis

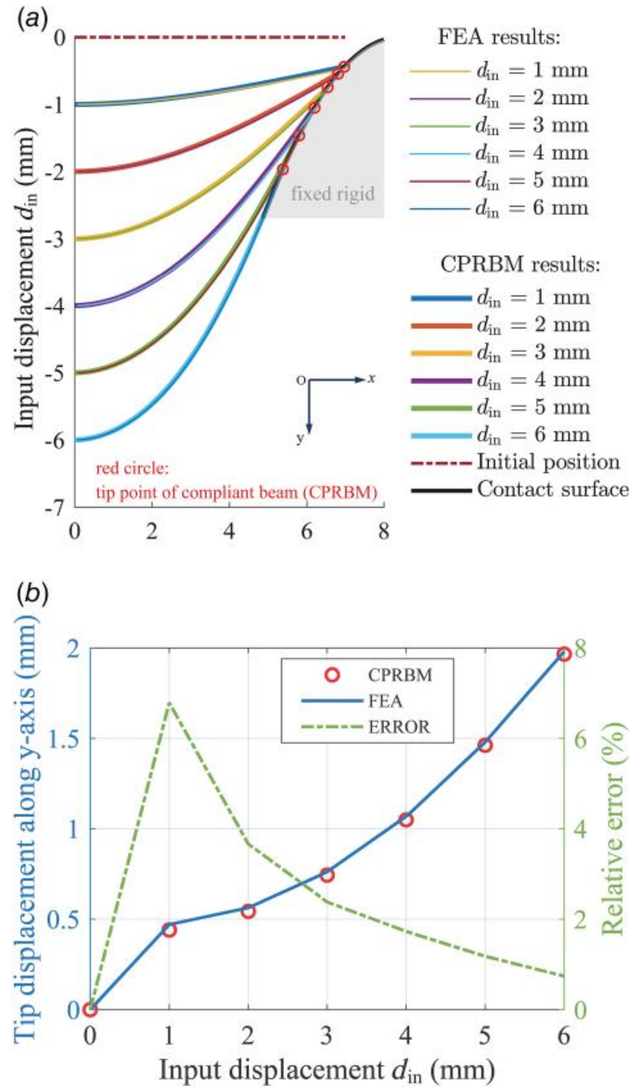

Fig. 8 Sheet-based CCFM with curved contact surface: (*a*) compliant beam interaction with curved contact surface and (*b*) its tip displacement along y-axis

input displacement of 1 mm. This larger deviation in the initial contact phase is mainly attributed to low load sensitivity, where small absolute displacement differences result in high relative errors, compounded by discretizations and contact-modeling effects in the FEA simulation. Specifically, the clearance between the compliant beam and the contact surface can lead to instability in the FEA results, thereby introducing error. In addition, the inherent limitations of the analytical model also affect the results. The CPRBM simplifies the compliant beam to its centerline; therefore, in the FEA, the contact surface needs to be offset downward by 0.2 mm (half of the compliant beam thickness) to correspond to the deformation predicted by the analytical model. However, the tip point of deformed compliant beam in FEA penetrates the contact surface defined in the CPRBM, which leads to relative errors. Finally, the contact position also influences the CPRBM results. The more contact points, the lower the relative error. During the initial contact phase, only the right end of the compliant beam touches the contact surface. As the input displacement increases and the beam enters the large-deflection regime, the contact evolves from a single point to two or more points. This explains why the analytical results show close agreement with the FEA results once the input displacement exceeds 2 mm for the linear contact surface and 1 mm for the curved contact surface. In the large-deflection phase, at an input displacement of 6 mm, the relative error drops below 3%, as shown in Figs. 7(*a*) and 7(*b*). This level of precision validates the accuracy of the analytical model based on CRPBM, which can precisely simulate the different deformation states of the compliant beam when accounting for various contact under different input displacements. The accuracy of the analytical model lays a solid foundation for the subsequent reaction force calculations.

Based on *fmincon* in MATLAB, the Lagrange multipliers are extracted to obtain the relationship between the input displacement and the reaction force of the sheet-based CCFM. The force–displacement relationships generated by the contact between a single compliant beam and the contact surface are shown in Fig. 9. Figures 9(*a*) and 9(*b*) illustrate the influence of different compliant beam thicknesses on the reaction force, where Fig. 9(*a*) corresponds to the linear contact surface defined by $C_1(5, -2.5)$ and $C_2(7, -0.2)$, Fig. 9(*b*) corresponds to the curved contact surface defined by $C_1(5, -2.5)$, $C_2(8.4, 0)$, and $C_3(11.8, -2.5)$. Figures 9(*c*) and 9(*d*) demonstrate the effects of different contact surface widths on the force–displacement relationship with a compliant beam thickness of $T = 0.4$ mm; Fig. 9(*c*) corresponds to the linear contact surface, and Fig. 9(*d*) to the curved contact surface. It can be observed that the reaction force increases with

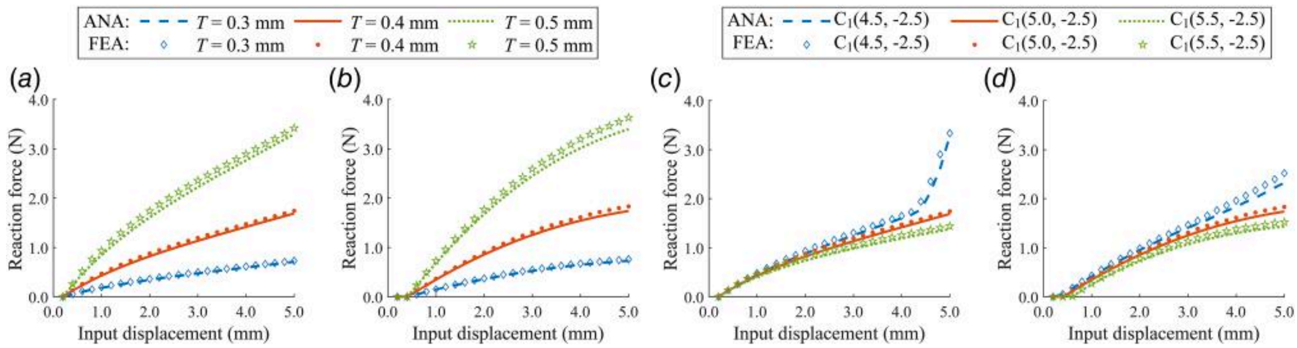

Fig. 9 Force–displacement characteristics of CCFM with one compliant beam: effects of compliant beam thickness for (*a*) linear and (*b*) curved contact surfaces, effects of contact surface width for (*c*) linear and (*d*) curved contact surfaces

increasing beam thickness and also increases as the contact surface width increases. When the beam thickness $T = 0.4$ mm and the linear or curved contact surfaces width are defined by $C_1(5, -2.5)$ and $C_3(11.8, -2.5)$, the reaction force produced by a single compliant beam at an input displacement $d_{\text{in}} = 5$ mm is 1.69 N for the linear contact surface. Since the compliant sheet consists of three such beams, the total reaction force becomes 5.07 N. Similarly, for the curved contact surface, a single compliant beam generates a reaction force of 1.74 N at the same input displacement, resulting in a total force of 5.22 N for the compliant sheet. Both results fall within the required maximum allowable force range (5–6 N). Nevertheless, a stress analysis is still necessary to ensure that the compliant beams do not fail during bending deformation.

According to the von Mises stress analysis shown in Fig. 10, for the linear contact surface, when the input displacement $d_{\text{in}} = 5$mm, the von Mises stresses at the root and the contact point of the compliant beam are 59.21 MPa and 91.81 MPa, respectively. For the curved contact surface, the two von Mises stresses are 66.96 MPa and 92.77 MPa. The von Mises stress in contact point is significantly higher than that at the beam root, which is attributed to the presence of strong localized (Hertz-type [38]) loading. The contact between the compliant beam and the contact surface occurs as either single-point or multipoint contact. The contact surface transfers the load to compliant beam through a very small contact area, resulting in a pronounced triaxial stress state near the surface (normal compressive stress combined with shear stress). The von Mises stress is highly sensitive to such localized multiaxial stress states and therefore reaches its maximum in contact point. Consequently, the von Mises stress at the root of the beam is adopted for safety factor calculation. Then the safety factors corresponding to the linear and curved contact surfaces are 1.86 and 1.64 (yield strength $\sigma_y = 110$ MPa of PEEK).

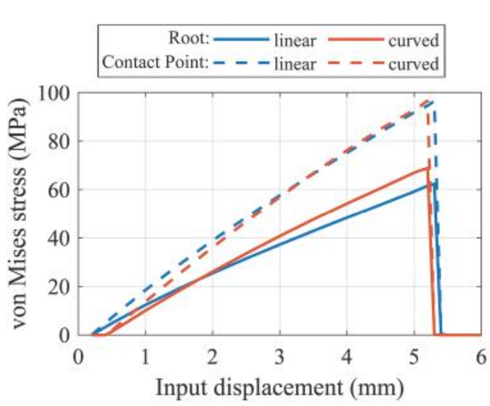

Fig. 10 Stress analysis of the sheet-based CCFM

Finally, the maximum contact point x_{max} is identified to realize the force-limiting function, representing the last position at which the compliant beam remains in contact with the contact surface. Once the beam passes this maximum contact point, it separates from the contact surface, causing the reaction force to drop abruptly to zero. Based on the analytical model, the contact position on the contact surface corresponding to an input displacement of 5 mm is first determined, and this position is x_{max}, as illustrated in Fig. 11. The maximum contact point for the linear contact surface is $x_{\text{max}}(5.85, -1.52)$, and for the curved contact surface, it is $x_{\text{max}}(5.80, -1.46)$. Subsequently, the entire force-limiting process is analyzed using ANSYS-based FEA, and the resulting force–displacement relationship is shown in Fig. 12. The maximum relative errors corresponding to the two contact surfaces are 9.3% and 6.8%, respectively, both occurring in the initial contact phase. These larger discrepancies are also attributed to the low load sensitivity in this regime, as well as the effects of discretizations and contact modeling in the FEA. Meanwhile, the deformation prediction results obtained from the CPRBM determine the accuracy of the Lagrangian operator. As input displacement increases, errors gradually reduce and eventually stabilize within the range of 3–5%.

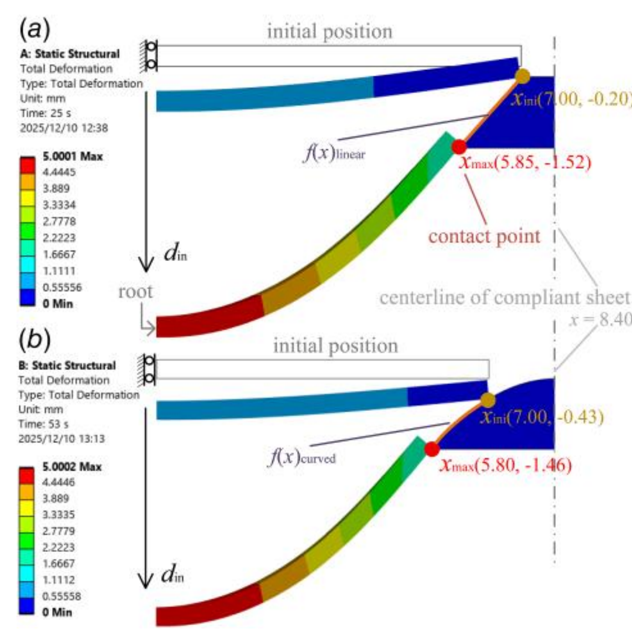

Fig. 11 Contact positions of the sheet-based CCFM with (*a*) linear and (*b*) curved contact surface

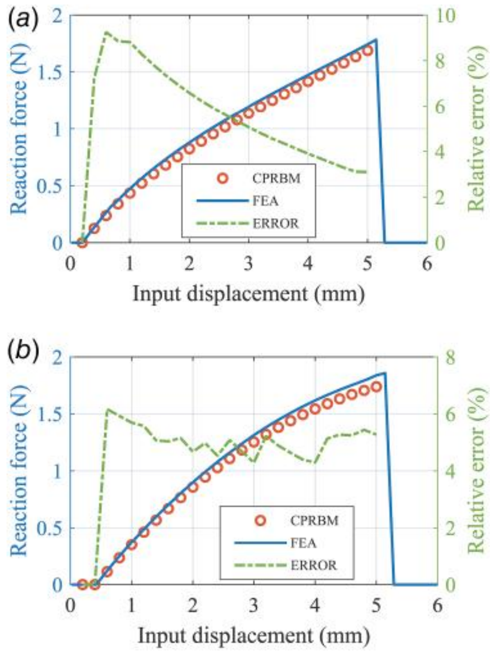

Fig. 12 Force-limiting characteristics of one compliant beam with (*a*) linear and (*b*) curved contact surface

5 Fabrication and Experimental Test

Several experimental tests are carried out for further verification of the proposed force-limiting applicator. The compliant sheet is made via laser cutting technology, with PEEK material, Young's modulus $E = 3600\,\text{MPa}$, Poisson's ratio $\mu = 0.38$, and yield strength $\sigma_y = 110\,\text{MPa}$. Except for the compliant sheet, all components of the applicator are fabricated using 3D printing. The contact rod and guide rod are printed using Rigid 4000 resin, which has a Young's modulus of $E = 3400\,\text{MPa}$. The smooth surface of this material further reduces the influence of surface friction on the experimental results. The geometric dimensions of the contact surface are designed based on the coordinates of the maximum contact point. For the linear contact surface, the initial contact point is $x_{\text{ini}}(7, -0.2)$ and the maximum contact point is $x_{\max}(5.85, -1.52)$. Thus, the contact surface height is determined as $h_{\text{linear}} = 1.32\,\text{mm}$, and the width $t_{\text{linear}} = 5.10\,\text{mm}$. To facilitate fabrication and repeated use (with the compliant rod head repeatedly passing through the compliant sheet), the contact rod head with a linear contact surface is designed as a two-part structure, in which the upper part forms the linear contact surface and the total height of the contact rod head is set to $h_{\text{head}} = 3.5\,\text{mm}$, as shown in Fig. 13. For the curved contact surface, the y-coordinate of the maximum contact point directly defines the contact surface height, resulting in $h_{\text{curved}} = 1.46\,\text{mm}$, and the width of contact surface is $t_{\text{curved}} = 5.20\,\text{mm}$. The specific geometric parameters of the sheet-based CCFM are listed in Table 1. The remaining components of the applicator, including the upper and outer cylinders as well as the base, are fabricated from Tough PLA.

For an accurate assembly of the compliant sheet, a positioning groove is incorporated between the outer cylinder and the upper cylinder. This groove not only aligns the compliant sheet but also provides an initial restraint against its rotation. To further secure the compliant sheet, the upper and outer cylinders are joined using screws inserted through three connection holes, with the nuts tightened to further ensure the compliant sheet is firmly fixed in place, as illustrated in Fig. 13. For the assembly of the force-limiting applicator, the contact rod is first positioned within the alignment groove located above the guide rod. The guide rod, together with the attached contact rod, is then inserted into the outer cylinder. Subsequently, the compliant sheet is placed into the positioning groove and the upper cylinder is secured. Finally, the base is installed beneath the guide rod.

The experimental setup employs the TA HD Plus texture analyzer, which allows precise displacement or force-controlled testing. To minimize ground vibrations, the base of the applicator is mounted on the texture analyzer testing platform. The probe is

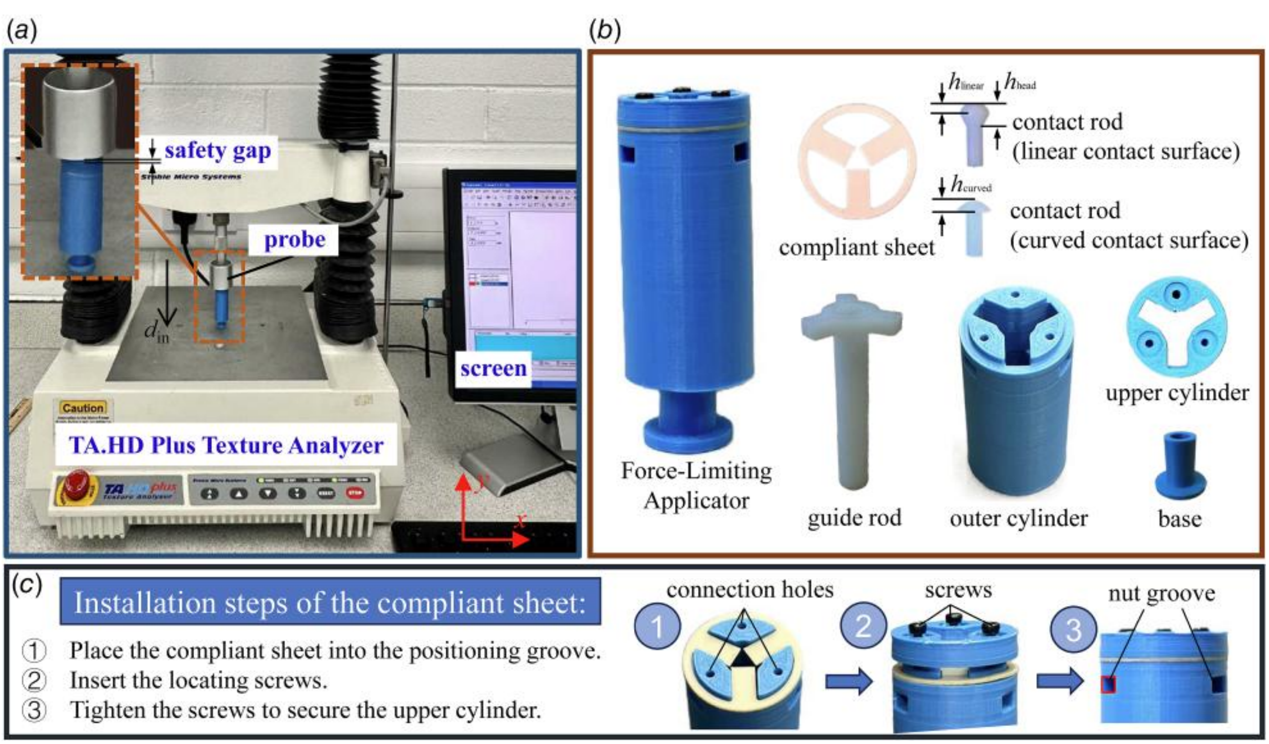

Fig. 13 Experimental testing: (*a*) experimental setup, (*b*) prototype components, and (c) installation steps

Table 1 Dimensions of the sheet-based CCFM

Parameter	Symbol	Value (mm)
Beam length	L	7.00
Beam width	W	4.00
Beam thickness	T	0.40
Outer diameter	D_{out}	20.00
Inner diameter	D_{in}	17.27
Linear contact surface	$f(x)_{linear}$	–
Linear surface height	h_{linear}	1.32
Contact head height	h_{head}	3.50
Linear surface width	t_{linear}	5.10
Curved contact surface	$f(x)_{curved}$	–
Curved surface height	h_{curved}	1.46
Curved surface width	t_{curved}	5.20
Contact rod length	l	7.00
Contact diameter	d	2.00

positioned at the upper end of the prototype, with a minimal safety gap maintained between the probe and the prototype to ensure safety redundancy. In this study, the texture analyzer applies a vertical downward displacement to the microneedle applicator through testing probe. The downward movement distance of the probe corresponds to the input displacement d_{in} of the sheet-based CCFM. The specific experimental setup can be found in Fig. 13.

To minimize dynamic effects, the loading speed during the experiment is set to 0.1 mm/s. Each test is repeated five times, and the averaged result is used as the experimental value. The specific results of the force–displacement characteristics are shown in Fig. 14. Since the sheet-based CCFM exhibits contact characteristics, its force-limiting performance is highly sensitive to friction between materials. Therefore, to better reflect practical operating conditions, three friction coefficients—0, 0.05, and 0.1—are adopted in the FEA and compared with the experimental results.

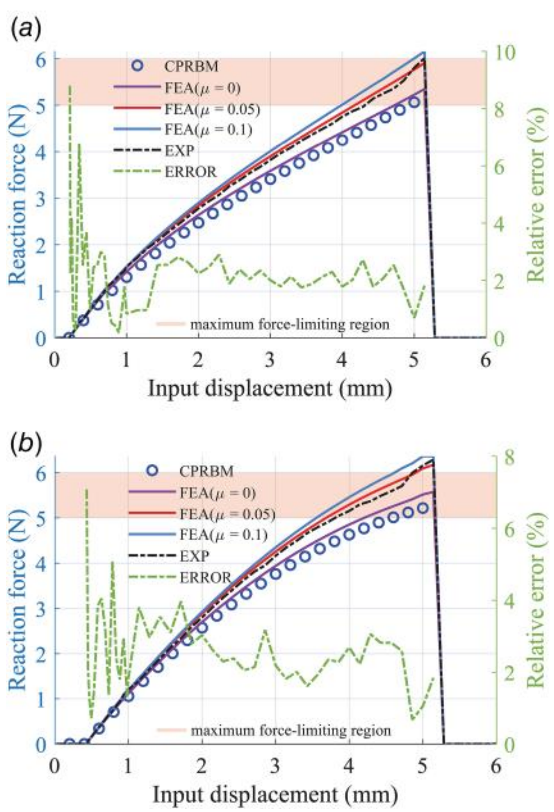

Fig. 14 Experimental results of force-limiting applicator with (*a*) linear and (*b*) curved contact surface

When the friction coefficient is set to $\mu = 0.05$, the FEA results show good agreement with the experimental data, with the maximum relative errors 8.80% and 7.08% occurring in the initial contact phase for the two different contact surfaces, respectively. In the large deformation region, the maximum relative errors for both contact surfaces remain below 4%. This discrepancy mainly results from assembly errors. In theoretical analysis, a clearance of 0.2 mm (refer to Fig. 2 for the definition of this clearance) is assigned between the compliant beam and the contact rod for the linear contact surface to prevent premature contact. However, in practical fabrication, this clearance cannot be precisely achieved due to manufacturing limitations. For the curved contact surface, the apex is required to coincide with the center of the compliant sheet, yet such alignment is difficult to realize in practice. These fabrication deviations lead to inconsistencies between the actual and theoretical contact points, thereby affecting the force–displacement characteristics obtained from experiments and introducing relative errors. In addition, the initial safety gap (Fig. 13) between the probe and the prototype further alters the actual contact location. Furthermore, the experimental results exhibit slightly greater fluctuations than the FEA predictions, mainly attributed to the inconsistency in surface roughness. To further improve manufacturing accuracy and reduce positioning errors, the contact rod and guide rod can be manufactured as an integrated component using injection molding or precision turning. In general, the experimental and FEA results exhibit consistent trends in reaction force versus displacement, where the force-limiting function is successfully achieved, further validating the feasibility of the proposed design.

6 Discussion

The operation process of the proposed force-limiting microneedle patch applicator and the corresponding working states of the sheet-based CCFM are illustrated in Fig. 15. The force-limiting applicator features a compact form that enables two-finger-handled operation. Its design is developed by integrating the analytical model with ANSYS-based FEA verification, and the detailed design procedure is presented in Fig. 16. The analytical model accurately predicts the deformation behavior of the compliant sheet as it interacts with different contact rods. A polynomial-based representation is employed to describe the contact surface, where varying contact surfaces can be generated by adjusting the coordinates of the control points. The force–displacement characteristics derived through the CRPBM with the help of the Lagrangian operator extraction accurately reflect the variation of the reaction force. Leveraging the deformation and force predictions provided by the analytical model, a wide range of sheet-based CCFM configurations can be systematically designed.

The theoretical model in this article is based on the CPRBM method, which offers simplicity, intuition, and convenience to solve contact problems. However, this method does not account for contact friction, which may lead to noticeable discrepancies

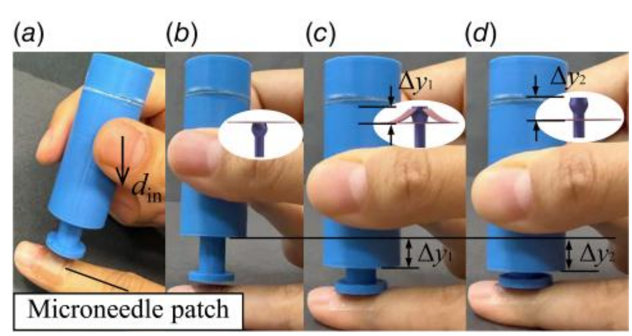

Fig. 15 Operation process of the force-limiting microneedle patch applicator

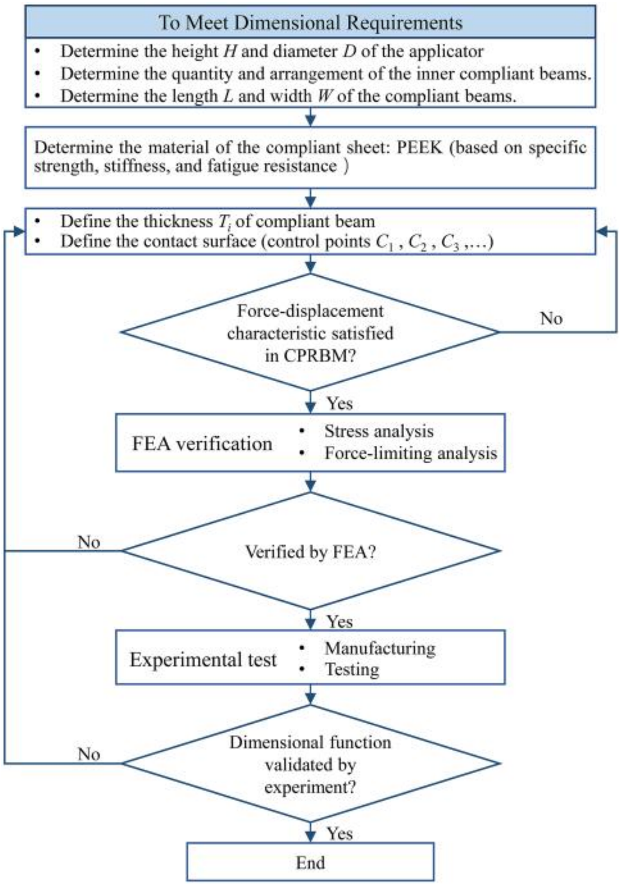

Fig. 16 Design procedure for the force-limiting microneedle patch applicator

between the theoretical predictions and the experimental results. To mitigate this limitation, in FEA, the friction coefficient in the contact definition is set to 0.05 to better approximate the actual contact behavior. In addition, the CPRBM method simplifies the compliant beam to its centerline, which introduces deviations in the prediction of beam deformation and force–displacement characteristics. As a result, the relative error in force prediction increases with increasing beam thickness T. Specifically, the maximum force prediction error of the linear contact surface is 8.2% for $T = 0.3$ mm, 9.3% for $T = 0.4$ mm, and 10.7% for $T = 0.5$ mm. Furthermore, in the FEA, the contact surface is shifted downward by $T/2$ to match the analytical model. This adjustment leads to discrepancies between the contact points in the FEA and those predicted by the analytical model, thereby introducing additional errors. With regard to the reaction forces, although they cannot be obtained from the CPRBM method directly, they can be evaluated using the Lagrange multiplier associated with the KKT conditions. The accuracy of this force prediction depends on the postcontact deformation state of the compliant sheet. Finally, because the CPRBM discretizes the beam into a number of identical straight segments, it is not suitable for compliant beams with variable cross sections.

The compliant sheet is fabricated using laser cutting, while all other components of the applicator are manufactured by 3D printing, resulting in low production cost and high manufacturing efficiency. In this study, the contact rod produced by 3D printing is made of Rigid 4000 resin. Although its contact surface is relatively smooth, inherent surface roughness still exists, which generates friction when in contact with the compliant sheet and consequently affects the force-limiting performance of the applicator. As shown in Fig. 14, with the increase of friction coefficient, the maximum limiting force also increases, and the nonlinear characteristics in the force–displacement relationship become less pronounced. When the friction coefficient $\mu = 0.05$, the FEA results agree better with the experiment results. Under this condition, the applicator with linear contact surface exhibits a maximum limiting force of 5.90 N, which lies within the maximum force-limiting region (5–6 N) [36,37], whereas the applicator with curved contact surface reaches a maximum limiting force of 6.17 N. In addition, as the force-limiting applicator is used repeatedly, the surface roughness of the contact interface slightly decreases, leading to a small reduction in the maximum limiting force. Therefore, in practical product development, it is recommended to characterize the friction at different stages of use to ensure that the maximum limiting force remains within the desired region. It is worth emphasizing that the force-limiting behavior of the proposed applicator is primarily dependent on the geometric configuration and elastic properties of the sheet-based CCFM. Therefore, even if friction is uncertain, stable force-limiting performance can still be achieved, demonstrating strong robustness in practical applications.

The force-limiting applicator proposed in this article is primarily designed for microneedle patches applied around the periungual skin, as shown in Fig. 15. The mechanical properties of skin can vary significantly with factors such as age, gender, and anatomical location. Even within the same region, different tissue layers exhibit distinct mechanical characteristics [7]. Variations in skin mechanics directly influence both the maximum insertion force of microneedles and the integrity of their penetration. Since the proposed applicator force-limiting process can induce a sudden release of force, this may cause skin rebound, affecting the integrity of microneedle insertion. To investigate the effect of force release on insertion integrity, optical coherence tomography can be employed to observe structural changes in the skin after microneedle insertion [39]. Additionally, the insertion process can be monitored by measuring the electrical impedance between microneedles and counter electrodes placed on the skin [40]. Furthermore, FEA of the relevant skin tissues can be conducted to explore variations in microneedle insertion positions [41]. In practical use, different microneedle patches require different insertion forces [42]. To enable the applicator to meet various force-limiting requirements, the maximum force limit can be adjusted by adopting compliant sheets with different parameters. Furthermore, the sheet-based CCFM can be optimized by adjusting the geometric structure of the compliant beam, for example to a trapezoidal shape. The process begins by identifying the specific force-limiting requirements based on the actual application scenario, followed by defining the optimization objectives, including the force increase trend, service life, size, and manufacturing cost of the mechanism.

7 Conclusions

This article proposes a force-limiting microneedle patch applicator that limits the maximum input force during microneedle insertion. The applicator features a compact structure, contains no electronic components, and offers low manufacturing cost and reusability. The force-limiting functionality is achieved through a sheet-based CCFM, consisting of a compliant sheet and a contact rod. In this mechanism, the contact rod interacts with three compliant beams within the compliant sheet, inducing different bending deformations to limit the maximum input force. An analytical model based on the CPRBM method is developed to predict the deformation of the compliant beam and the corresponding beam–rod contact positions. Based on the deformation prediction results, the force–displacement relationship is derived using the Lagrange operator extraction approach. Both linear and curved contact surfaces are analyzed, and the analytical results show good agreement with the FEA results. A prototype of the applicator is fabricated and experimentally tested. FEA is conducted to evaluate the force–displacement relationships under different friction coefficients. The results show that when the friction coefficient $\mu = 0.05$, the FEA results agree well with the experimental results, further validating the effectiveness of the proposed design. In addition, the practical application, design procedure, analytical model limitations, the influence of friction, and the effect of the force-limiting process on microneedle insertion integrity are discussed, followed by an outline of potential directions for future optimization. Overall, the proposed force-limiting microneedle patch applicator demonstrates a novel and effective use of contact-aided compliant mechanisms, offering new opportunities for safe and reliable microneedle delivery.

Acknowledgment

The authors sincerely appreciate the microneedle patches and financial support from Dr. Walid Faisal at the School of Pharmacy, UCC, as well as the assistance from Timothy Power and Zhengyao Wang at the School of Engineering and Architecture, UCC, in prototype fabrication and experimental testing.

Conflict of Interest

There are no conflicts of interest.

Data Availability Statement

The datasets generated and supporting the findings of this article are obtainable from the corresponding author upon reasonable request.

References

[1] Trejos, A., Patel, R., and Naish, M., 2010, "Force Sensing and Its Application in Minimally Invasive Surgery and Therapy: A Survey," Proc. Inst. Mech. Eng., Part C: J. Mech. Eng. Sci., **224**(7), pp. 1435–1454.

[2] Zhang, S., Guo, S., Fu, Y., Boulardot, L., Huang, Q., Hirata, H., and Ishihara, H., 2017, "Integrating Compliant Actuator and Torque Limiter Mechanism for Safe Home-Based Upper-Limb Rehabilitation Device Design," J. Med. Biol. Eng., **37**(3), pp. 357–364.

[3] Lauzier, N., and Gosselin, C., 2010, "3-Dof Cartesian Force Limiting Device Based on the Delta Architecture for Safe Physical Human-Robot Interaction," IEEE International Conference on Robotics and Automation, Anchorage, AK, May 3–7, IEEE, pp. 3420–3425.

[4] Puangmali, P., Althoefer, K., Seneviratne, L. D., Murphy, D., and Dasgupta, P., 2008, "State-of-the-Art in Force and Tactile Sensing for Minimally Invasive Surgery," IEEE Sens. J., **8**(4), pp. 371–381.

[5] Reinke, A., Whiteside, E. J., Windus, L., Desai, D., Stehr, E., and Rad, Z. F., 2024, "The Advantages of Microneedle Patches Compared to Conventional Needle-Based Drug Delivery and Biopsy Devices in Medicine," Biomed. Eng. Adv., **8**, p. 100127.

[6] Norman, J. J., Arya, J. M., McClain, M. A., Frew, P. M., Meltzer, M. I., and Prausnitz, M. R., 2014, "Microneedle Patches: Usability and Acceptability for Self-Vaccination Against Influenza," Vaccine, **32**(16), pp. 1856–1862.

[7] Makvandi, P., Kirkby, M., Hutton, A. R., Shabani, M., Yiu, C. K., Baghbantaraghdari, Z., and Jamaledin, R., 2021, "Engineering Microneedle Patches for Improved Penetration: Analysis, Skin Models and Factors Affecting Needle Insertion," Nano-Micro Lett., **13**(1), pp. 1–41.

[8] Wei, Y., and Xu, Q., 2015, "An Overview of Micro-Force Sensing Techniques," Sens. Actuators A: Phys., **234**, pp. 359–374.

[9] Xu, K., and Simaan, N., 2008, "An Investigation of the Intrinsic Force Sensing Capabilities of Continuum Robots," IEEE Trans. Rob., **24**(3), pp. 576–587.

[10] Gil, B., Li, B., Gao, A., and Yang, G.-Z., 2020, "Miniaturized Piezo Force Sensor for a Medical Catheter and Implantable Device," ACS Appl. Electronic Mater., **2**(8), pp. 2669–2677.

[11] Howell, L. L., 2013, "Compliant Mechanisms," *21st Century Kinematic*, Springer, p. London, p. 189–216.

[12] Fontanelli, G. A., Buonocore, L. R., Ficuciello, F., Villani, L., and Siciliano, B., 2020, "An External Force Sensing System for Minimally Invasive Robotic Surgery," IEEE/ASME Trans. Mech., **25**(3), pp. 1543–1554.

[13] Chen, Y.-H., and Lan, C.-C., 2012, "An Adjustable Constant-Force Mechanism for Adaptive End-Effector Operations," ASME J. Mech. Des., **134**(3), p. 031005.

[14] Pham, H.-T., and Wang, D.-A., 2011, "A Constant-Force Bistable Mechanism for Force Regulation and Overload Protection," Mech. Mach. Theory, **46**(7), pp. 899–909.

[15] Zhang, Q., Yan, P., and Wang, H., 2022, "A Curved-Beam Based Quasi-Constant Force Mechanism Supporting Large Range and Force-Sensitive Robotic Manipulation," Mech. Mach. Theory, **172**, p. 104799.

[16] Miao, Y., and Zheng, J., 2020, "Optimization Design of Compliant Constant-Force Mechanism for Apple Picking Actuator," Comput. Electron. Agricul., **170**, p. 105232.

[17] Slocum, J., Kamrin, K., and Slocum, A., 2019, "A Buckling Flexure-Based Force-Limiting Mechanism," ASME J. Mech. Rob., **11**(4), p. 041004.

[18] Dobrokhotov, V. V., Yazdanpanah, M. M., Pabba, S., Safir, A., and Cohn, R. W., 2007, "Visual Force Sensing With Flexible Nanowire Buckling Springs," Nanotechnology, **19**(3), p. 035502.

[19] An, S., Kim, B., Kwon, S., Moon, G., Lee, M., and Jhe, W., 2018, "Bifurcation-Enhanced Ultrahigh Sensitivity of a Buckled Cantilever," Proc. Natl. Acad. Sci. U. S. A., **115**(12), pp. 2884–2889.

[20] Noda, S., Tokuoka, Y., Kuriu, S., and Ishida, T., 2022, "Proposal of Forceps Force Limiter Design Using Leaf Spring Buckling," Robomech J., **9**(1), p. 3.

[21] Heimberger, R., and Schaumann, U., 1996, "Forceps," U.S. Patent No. 5,562,699.

[22] Mankame, N. D., and Ananthasuresh, G., 2002, "Contact Aided Compliant Mechanisms: Concept and Preliminaries," International Design Engineering Technical Conferences and Computers and Information in Engineering Conference, Montreal, Quebec, Canada, Sept. 29–Oct. 2, Vol. 36533, American Society of Mechanical Engineers, pp. 109–121.

[23] Saxena, A., 2013, "A Contact-Aided Compliant Displacement-Delimited Gripper Manipulator," ASME J. Mech. Rob., **5**(4), p. 041005.

[24] Yao, J., Fang, Y., Yang, X., Wang, P., and Li, L., 2024, "Design Optimization of Soft Robotic Fingers Biologically Inspired by the Fin Ray Effect With Intrinsic Force Sensing," Mech. Mach. Theory, **191**, p. 105472.

[25] Cannon, J. R., and Howell, L. L., 2005, "A Compliant Contact-Aided Revolute Joint," Mech. Mach. Theory, **40**(11), pp. 1273–1293.

[26] Jin, M., Yang, Z., Ynchausti, C., Zhu, B., Zhang, X., and Howell, L. L., 2020, "Large-Deflection Analysis of General Beams in Contact-Aided Compliant Mechanisms Using Chained Pseudo-Rigid-Body Model," ASME J. Mech. Rob., **12**(3), p. 031005.

[27] Chen, G., Ma, F., Hao, G., and Zhu, W., 2019, "Modeling Large Deflections of Initially Curved Beams in Compliant Mechanisms Using Chained Beam Constraint Model," ASME J. Mech. Rob., **11**(1), p. 011002.

[28] Pauly, J., and Midha, A., 2006, "Pseudo-Rigid-Body Model Chain Algorithm: Part 1—Introduction and Concept Development," International Design Engineering Technical Conferences and Computers and Information in Engineering Conference, Philadelphia, PA, Sept. 10–13, Vol. 42568, pp. 173–181.

[29] Pauly, J., and Midha, A., 2006, "Pseudo-Rigid-Body Model Chain Algorithm: Part 2—Equivalent Representations for Combined Load Boundary Conditions," International Design Engineering Technical Conferences and Computers and Information in Engineering Conference, Philadelphia, PA, Sept. 10–13, Vol. 42568, pp. 183–190.

[30] Rao, S. S., 2018, *The Finite Element Method in Engineering*, 6 ed., Elsevier Butterworth-Heinemann, Oxford, UK, pp. 295–330.

[31] Venkateshan, S., and Swaminathan, P., 2014, "Boundary Value Problems (ODE)." Computational Methods in Engineering, S. Venkateshan and P. Swaminathan, eds. Academic Press, Boston, pp. 447–512.

[32] Qiu, L., Dai, S., Li, Y., and Li, C., 2022, "Design and Analysis of a Contact-Aided Leaf Hinge (CALH) With Continuous Variable Stiffness," Mech. Mach. Theory, **169**, p. 104653.

[33] Wang, Y., Dai, S., He, X., and Hao, G., 2025, "Design of a Sheet Based Contact-Aided Compliant Force-Limiting Mechanism for Microneedle Patch Applicators," International Design Engineering Technical Conferences and Computers and Information in Engineering Conference, Anaheim, CA, Aug. 17–20.

[34] Guo, L., Allen, J. K., and Mistree, F., 2024, "Optimize or Satisfice in Engineering Design?" Res. Eng. Des., **35**(3), pp. 239–267.

[35] Sartawi, Z., Blackshields, C., and Faisal, W., 2022, "Dissolving Microneedles: Applications and Growing Therapeutic Potential," J. Controlled Release, **348**, pp. 186–205.

[36] Davis, S. P., Landis, B. J., Adams, Z. H., Allen, M. G., and Prausnitz, M. R., 2004, "Insertion of Microneedles Into Skin: Measurement and Prediction of Insertion Force and Needle Fracture Force," J. Biomech., **37**(8), pp. 1155–1163.

[37] Park, S. C., Kim, M. J., Baek, S. -K., Park, J. -H., and Choi, S. -O., 2019, "Spray-Formed Layered Polymer Microneedles for Controlled Biphasic Drug Delivery," Polymers, **11**(2).

[38] Gonzalez-Perez, I., Iserte, J. L., and Fuentes, A., 2011, "Implementation of Hertz Theory and Validation of a Finite Element Model for Stress Analysis of Gear Drives With Localized Bearing Contact," Mech. Mach. Theory, **46**(6), pp. 765–783.

[39] Coulman, S. A., Birchall, J. C., Alex, A., Pearton, M., Hofer, B., O'Mahony, C., Drexler, W., and Považay, B., 2011, "In Vivo, In Situ Imaging of Microneedle Insertion Into the Skin of Human Volunteers Using Optical Coherence Tomography," Pharm. Res., **28**(1), pp. 66–81.

[40] Roxhed, N., Gasser, T. C., Griss, P., Holzapfel, G. A., and Stemme, G., 2007, "Penetration-Enhanced Ultrasharp Microneedles and Prediction on Skin Interaction for Efficient Transdermal Drug Delivery," J. Microelectromech. Syst., **16**(6), pp. 1429–1440.

[41] Shu, W., Heimark, H., Bertollo, N., Tobin, D. J., O'Cearbhaill, E. D., and Annaidh, A. N., 2021, "Insights Into the Mechanics of Solid Conical Microneedle Array Insertion Into Skin Using the Finite Element Method," Acta Biomater., **135**, pp. 403–413.

[42] Olatunji, O., Das, D. B., Garland, M. J., Belaid, L., and Donnelly, R. F., 2013, "Influence of Array Interspacing on the Force Required for Successful Microneedle Skin Penetration: Theoretical and Practical Approaches," J. Pharm. Sci., **102**(4), pp. 1209–1221.